Research Article | Vol. 30, No. 24 / 21 Nov 2022 / Optics Express 42995
Optics EXPRESS

Multi-material spectral photon-counting micro-CT with minimum residual decomposition and self-supervised deep denoising

V. Di Trapani,[1] L. Brombal,[2,*] and F. Brun[2,3]

[1]Department of Physics, University of Trieste, Via A. Valerio 2, 34127 Trieste, Italy
[2]Division of Trieste, National Institute for Nuclear Physics (INFN), Via A. Valerio 2, 34127, Trieste, Italy
[3]Department of Engineering and Architecture, University of Trieste, Via A. Valerio 6, 34127 Trieste, Italy
*luca.brombal@ts.infn.it

Abstract: Spectral micro-CT imaging with direct-detection energy discriminating photon counting detectors having small pixel size (< 100×100 μm^2) is mainly hampered by: i) the limited energy resolution of the imaging device due to charge sharing effects and ii) the unavoidable noise amplification in the images resulting from basis material decomposition. In this work, we present a cone-beam micro-CT setup that includes a CdTe photon counting detector implementing a charge summing hardware solution to correct for the charge-sharing issue and an innovative image processing pipeline based on accurate modeling of the spectral response of the imaging system, an improved basis material decomposition (BMD) algorithm named minimum-residual BMD (MR-BMD), and self-supervised deep convolutional denoising. Experimental tomographic projections having a pixel size of 45×45 μm^2 of a plastinated mouse sample including I, Ba, and Gd small cuvettes were acquired. Results demonstrate the capability of the combined hardware and software tools to sharply discriminate even between materials having their K-Edge separated by a few keV, such as e.g., I and Ba. By evaluating the quality of the reconstructed decomposed images (water, bone, I, Ba, and Gd), the quantitative performances of the spectral system are here assessed and discussed.

1. Introduction

The advent of photon-counting detectors (PCD) is revolutionizing X-ray spectral computed tomography (CT) in pre-clinical and clinical imaging applications [1,2]. Compared to spectral CT systems relying on dual X-ray sources or dual layer detectors, the adoption of PCD devices brings a simplification in the hardware and, by employing a broad X-ray spectrum, allows to target applications making use of different contrast media by simply adjusting the acquisition thresholds. Furthermore, the possibility of acquiring images over multiple energy bins, ideally in a single shot, enables for multi-material differentiation. In this context, the simultaneous use of different contrast agents (e.g., iodine – I, barium – Ba, gadolinium – Gd) is regarded as key to improving functional and multi-organ imaging applications [3,4]. For instance, the joint administration of I and Gd has been proposed in the study of tumor vasculature [5], for cardiovascular imaging [6], for colonography [7], and for quantitative abdominal imaging [8–11], whereas I and Ba can be used for simultaneous cardiovascular and gastrointestinal imaging [12].

Current PCD devices implement semiconductor sensors (typically, Si, GaAs, CdTe, or CdZnTe) where primary X-rays interact through photo-electric or scattering effects. The energy released in these interactions is converted into electron-hole pairs that drift under an electric potential in the order of a few hundred volts, generating an electrical signal. When the signal amplitude exceeds a programmable and energy-calibrated threshold value, an event is counted. By using multiple thresholds, events can be grouped into energy bins, therefore providing spectral information. When targeting high energy (>30 keV) applications, a high-Z sensor such as CdTe or CdZnTe

#471439 https://doi.org/10.1364/OE.471439
Journal © 2022 Received 24 Jul 2022; revised 1 Sep 2022; accepted 5 Sep 2022; published 8 Nov 2022

Optics EXPRESS

must be used to achieve a sufficient absorption efficiency. On the downside, if compared to Si semiconductors, high-Z sensors often present defects and impurities [13,14], which induce inhomogeneities in the images that must be properly treated with dedicated pre-processing procedures [15–17]. Commonly used materials, such as CdTe, generate high-energy fluorescence photons (in the range 23 - 27 keV for CdTe), altering the spectral response of the detection system. Moreover, when considering devices with a small pixel size (< 100×100 μm^2), required by high-resolution pre-clinical applications, charge sharing effects become predominant, negatively affecting spatial and, more importantly, energy resolution. Many modern chips, such as Medipix3 and Pixie-III, mitigate charge-sharing through a dedicated hardware processing at pixel level where signals due to charge released among neighboring pixels are summed prior to energy discrimination, thus restoring the full energy signal [18,19]. On the other hand, events associated with K-fluorescence or Compton escape where the energy is deposited far from the primary interaction point, cannot be compensated, thus contributing to a low energy component in the spectral response. All these effects, summed to the readout electronic noise, determine the final spectral performance of the detector and must be thoroughly modelled to perform accurate material discrimination and quantification.

In spectral imaging, material quantification is typically performed via basis material decomposition (BMD) [20] algorithms. Through BMD, the images collected at given energy bins are modelled as weighted sum of known energy-dependent functions (bases), where the weights are energy-independent scalar numbers. When dealing with contrast media embedded in biological samples, it is common practice to choose as basis functions their energy-dependent mass attenuation coefficients together with one representative of biological tissues (e.g., water), which is also referred to as non-contrast channel. Upon system calibration, this choice allows to express the weights in terms of absolute mass density. Given a sufficient number of energy bins, the linear system can be inverted to provide a 3D density map of each basis material. As with all matrix inversion algorithms, when applied to real, noisy data, BMD amplifies the input noise [11,21]. Therefore, the noise-transfer behavior of BMD may hamper a proper material discrimination/quantification by leading to cross-talk between the decomposed images and high noise levels. This issue is considerably enhanced when aiming at decomposing >2 materials [21]. To mitigate these effects, a plethora of matrix inversion strategies based on constrained minimization [22], spatio-spectral filtration [23], principal component analysis [24], single-step [25], multistep [26] and hybrid [27] approaches have been proposed. In this work, an alternative approach for multi-material discrimination, called minimum residual BMD (MR-BMD) is introduced. The algorithm uses all the available energy bins to identify the main elements in each reconstructed voxel prior the actual BMD. This additional step, allows for a local reduction of the number of bases employed in the BMD, with a consequent improvement in terms of material discrimination (cross-talk removal) and noise response.

Considering the noise-transfer behavior of BMD algorithms, the combined use with denoising strategies is critical for quantitative spectral CT [11,28–30]. In this field, denoising approaches which require no priors on the signal and no estimate of the noise are particularly attractive. To be specific, deep learning methods based on convolutional neural networks currently give state-of-the-art results, albeit being computationally intensive. These methods consider a first training step and a subsequent application (or prediction) to the noisy images. The most interesting difference among these methods relies on the set of images considered during the training step. If noisy and clean measurements of the same target are available, then supervised deep image denoising [31], sometimes called *Noise2Truth*, is an interesting option. When clean pairs are not available, then *Noise2Noise* (N2N) [32] has been proved to be a powerful tool, provided that multiple noisy images of the same target are available. When only one single image (without independent repetitions) is available, then *Noise2Self* [33] or *Noise2Void* [34] are most likely the options to consider, the latter being more interesting for scientific imaging. Since in

Optics EXPRESS

practical imaging clean targets are not available but repeated acquisitions are instead feasible, *Noise2Noise* results very attractive and its application to tomographic reconstruction has been investigated in e.g., [35]. Recently, a modified version of *Noise2Noise* called *Noise2Inverse* (N2I) has been proposed for the specific case of computed tomography [36]. The underlying idea of *Noise2Inverse* is to split the set of projections into independent subsets and proceed with an angularly registered reconstruction of these subsets, as applied for instance in [30,37]. These reconstructed subsets are the input of a convolutional neural network denoiser.

In this work, we introduce a micro-CT setup enabling the simultaneous differentiation and quantification of I-, Ba- and Gd-based contrast media from biological soft and hard tissue. A significant contribution of this work comes from the consideration of experimental images acquired with a small pixel size (i.e., 62 μm) CdTe photon-counting detector named Pixirad-1/Pixie-III in two-color mode. Pixirad-1/Pixie-III has already been successfully used in several applications of spectral imaging [38–42]. Considering a simple evolution where hardware re-binning allows for eight energy thresholds per macro-pixel [43], this work considers four consecutive two-color acquisitions in order to derive eight energy bins. An innovative digital image processing pipeline featuring an accurate spectral model of the system, a two-pass application of *Noise2Inverse* and *Noise2Noise*, and the MR-BMD algorithm is here presented. By considering a suitable test object conceived for small animal imaging, the performance of the denoising, as well as the advantages of the proposed MR-BMD over the standard BMD approach, are evaluated in terms of concentration (mg/ml) and signal-to-noise of the reconstructed contrast media in the decomposed images.

2. Materials and methods

2.1. Experimental setup: acquisition and reconstruction

Tomographic scans were acquired with a Pixirad-1/Pixie-III detector [19], implementing a 650 μm thick CdTe sensor bump bonded on a 512 × 402 matrix of pixels with a size of 62 × 62 μm^2, corresponding to an active area of 31.7 × 24.9 mm^2 and a linearity limit of 2.5×10^7 photons/s/mm^2 [44]. The detector and the sample were positioned at 58 cm and 42 cm from the X-ray source, respectively, corresponding to a geometrical magnification of 1.38. Since the width of the scanned sample was bigger than the width of the detector (considering the magnification), the detector was horizontally displaced by approximately 30% of its width with respect to the sample's rotation axis, and the projections were collected on a full 360° rotation. Reconstruction via conventional cone-beam FDK [45] with Shepp-Logan filtering and detector displacement weighting [46] has been performed by using the implementation available in the open source software library TIGRE [47]. The reconstructed volume is composed of 690 × 690 × 402 voxels with an isotropic voxel size of 45 × 45 × 45 μm^3. The Hamamamtsu L10101 microfocus X-ray source has been used at 70 kVp and current of 200 μA, with an added filtration of 0.12 mm of Cu and 0.20 mm of Al, corresponding to a flux at detector position of approximately 5×10^5 photons/s/mm^2, thus comfortably within the detector's linearity range.

The exposure time was 2 s per projection and five repetitive shots of the same projection were acquired, thus to perform projection averaging. A total number of 1440 projections were collected by exploiting the two color mode of the detector, i.e. the possibility to set two energy thresholds E_1 and E_2, thus to collect in a single shot the energy bins $[E_1, E_2[$ and $[E_2, +\infty[$. For each projection, four consecutive acquisitions were performed with modified values of E_1 and E_2. Thanks to simple digital pixel-by-pixel subtraction, the following eight energy datasets were derived: [21,26[, [26,33[, [33,37[, [37,43[, [43,47[, [47,51[, [50,57[, [57,70] keV. To limit ring artifacts in the reconstructed images, the detector was randomly displaced horizontally at each angular position (jittering) in a range between −6 and +6 pixels. The acquired projections were pre-processed with a refined flat-field correction that resolves defective and miscalibrated pixels [16,17]. An additional simple ring removal algorithm [48] has been also applied.

Optics EXPRESS

The scanned sample was composed of a plasticized mouse (PlastiMouse by SmART Scientific Solutions) positioned within a cylindrical holder together with 3 pipettes containing water solutions of I-, Ba- and Gd-based contrast agents with concentrations of 40, 35, and 39 mg/ml, respectively, as shown in Fig. 2(d). A sample reconstructed slice for each energy bin is reported in Fig. 1.

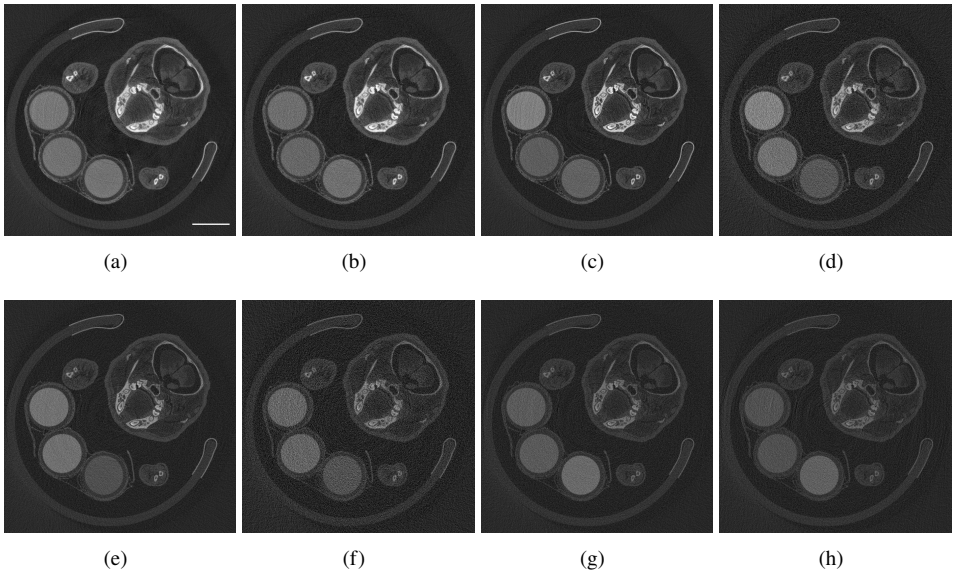

Fig. 1. Sample reconstructed slice of each energy bin: a) [21,26[keV; b) [26,33[keV; c) [33,37[keV; d) [37,43[keV; e) [43,47[keV; f) [47,51[keV; g) [51,57[keV; h) [57,70] keV. [The same window/level is used for each image. Scale bar is 5 mm]

2.2. Spectral system modelling

The estimation of the basis materials coefficients requires a careful modelling of the imaging system, both in terms of detector's energy response and X-ray spectrum. To this end, the spectral photon-counting detector used in this study, Pixirad-1/Pixie-III, has been thoroughly characterized with monochromatic synchrotron radiation [44,49]. The measured full-energy peak resolution, ranging from 3.6 to 4.1 keV at X-ray energies from 26 to 50 keV [44], was used as input to a Geant4-based Monte Carlo simulation [50,51]. The simulation includes all the X-ray/matter interactions within the CdTe sensor, i.e. fluorescence, escape and Compton scattering, in addition to a 4-neighboring pixels clustering mechanism mimicking the charge sharing compensation system integrated in the detector's electronics. The simulation has been validated against experimental data, as shown in Fig. 2(a), demonstrating its ability to reproduce the detector spectral features. By performing a fine energy scanning, the detector response has been subsequently simulated in a broad range from 10 to 100 keV, enabling the computation of the energy response for arbitrary energy bins and X-ray spectra [50]. Figure 2(b) shows the energy bins collected by the PCD, including the simulated CdTe response, for the spectrum and threshold settings employed in this work. From the figure, where the energy thresholds and the X-ray spectrum used in the experiment are considered, it should be noted that for low energy bins, e.g. the [21, 26[keV bin, a large fraction of the registered counts is associated to high energy X-rays due to fluorescence and escape photons. This high-energy contamination is particularly relevant in PCDs featuring small pixel size where it is more likely that fluorescence photons induced within the CdTe sensor are detected far from the point where the primary interaction

Optics EXPRESS

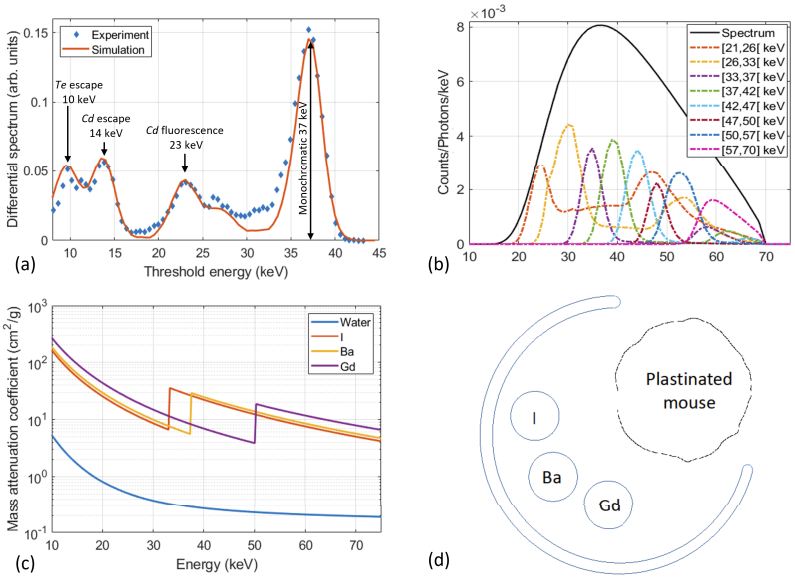

Fig. 2. (a) comparison between the simulated [50] and experimental differential spectra [44] obtained with the Pixirad/pixie-III PCD at $E = 37$ *keV*; (b) plot of the simulated input spectrum for a tungsten anode at 70 kVp, and the energy bins collected by the PCD including the simulated CdTe response; (c) plot of the mass attenuation coefficients for water, I, Ba, and Gd in the considered energy range; (d) sketch of the sample used for the experimental acquisition (the nominal concentrations of the k-edge elements were 40 mg/ml for I, 35 mg/ml for Ba, and 39 mg/ml for Gd).

occurs, thus being treated as independent events. The X-ray spectra have been simulated through the SpekCalc software [52].

2.3. *Spectral image processing*

For each energy bin, micro-CT images were derived by applying the following image processing pipelines, as depicted in Fig. 3:

- **No denoising**: conventional FDK reconstruction is performed and then BMD is applied in the reconstructed domain (without any additional denoising step);
- **Single-pass**: each projection dataset (where each projection results from the average of multiple repetitions of the same acquisition) is split into 4 angularly interleaved subsets and reconstruction plus *Noise2Inverse* (N2I) for each energy bin is performed. Then BMD is applied to the (denoised) reconstructed slices;
- **Two-pass**: since projection repetition is performed during acquisition, each single (not averaged) projection is the input for a single-pass approach as described before, followed by FDK reconstruction and BMD. After that, a final application of *Noise2Noise* (N2N) to the multiple decomposed images is performed.

For all the processing pipelines, two different basis material decomposition (BMD) methods are compared and hereafter described: conventional BMD and a proposed method named minimum residual BMD (MR-BMD).

Optics EXPRESS

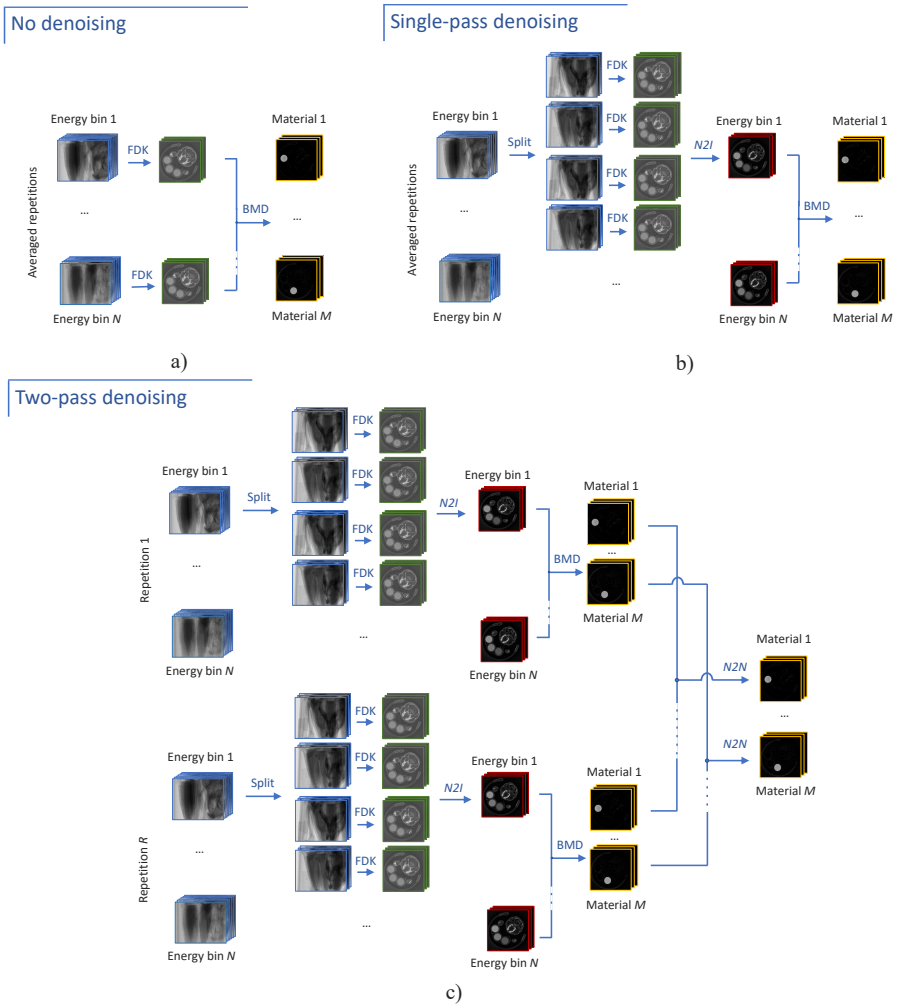

Fig. 3. Image processing pipelines considered in the manuscript: a) no denoising; b) the set of averaged projections is split into 4 subsets and *Noise2Inverse* (N2I) prior to basis material decomposition (BMD) is applied; c) each repetition of the set of projections is split in 4 subsets and *Noise2Inverse* (N2I) is applied followed by basis material decomposition (BMD), similarly to single-pass denoising. The denoised repetitions are then considered for a final application of *Noise2Noise* (N2N).

Optics EXPRESS

2.4. Spectral decomposition algorithms

The underlying idea of the BMD algorithm is to consider that the signal (V) measured within each voxel ($\vec{v}$) of a CT image can be written as a linear combination of basis functions:

$$V(\vec{v})_j = \sum_i \langle f \rangle_{i,j} \cdot \rho_i(\vec{v}) \tag{1}$$

where $\rho_i(\vec{v})$ is the unknown density of the i-th basis material and the $\langle f \rangle_{i,j}$ is the effective mass attenuation coefficient of the i-th basis material computed over the j-th energy bin as:

$$\langle f \rangle_{i,j} = \frac{\int \left(\frac{\mu(E)}{\rho}\right)_i S_j(E) dE}{\int S_j(E) dE} \tag{2}$$

In Eq. (2) the integral runs over the energy content of the j-th bin, entirely described by its energy dependence S_j, which encompasses both detector spectral response and the input X-ray spectrum. Considering a real PCD, as shown in Fig. 2 b, the energy bins $S_j(E)$ may extend outside the nominal width. By collecting n energy bins, Eq. (1) can be rewritten in matrix form:

$$\begin{pmatrix} V(\vec{v})_1 \\ \vdots \\ V(\vec{v})_n \end{pmatrix} = \begin{pmatrix} \langle f \rangle_{1,1} \cdots \langle f \rangle_{1,m} \\ \vdots \\ \langle f \rangle_{n,1} \cdots \langle f \rangle_{n,m} \end{pmatrix} \cdot \begin{pmatrix} \rho_1 \\ \vdots \\ \rho_m \end{pmatrix} \tag{3}$$

In the basic formulation of BMD algorithm, the density maps for each desired material is obtained through a least-squares matrix inversion of the $n \times m$ matrix ($\mathbf{M}$) of the weighted mass attenuation coefficients in Eq. (3).

In this work we propose a modified version of the standard BMD approach here referred to as MR-BMD (minimum residual-BMD). The MR-BMD algorithm exploits the multiple energy bins collectible with a PCD implementing multiple thresholds to first identify the materials and then reduce the number of bases to be employed in the BMD algorithm on a single voxel basis. The basic idea of the algorithm can be summarized as follows: (i) for each voxel the spectral data $V(\vec{v}, E)$ are extracted; (ii) the least-squares solution of the decomposition with a single material/element is computed for each basis; (iii) the basis which minimizes the residuals in step (ii) identifies the main material present in the selected voxel; (iv) the BMD is then restricted to the detected material. In this latter stage, if the detected material is a k-edge element the BMD is restricted to two bases including water and the detected k-edge element. The pseudo-code of MR-BMD is included in this manuscript. The MR-BMD algorithm described above considers the experimental case where contrast agents are spatially separated. When considering a more complex case where a voxel may include a mixture of k-edge elements, the algorithm can be easily generalized by inserting the expected mixture as a basis in stage (ii). In this case, the residuals of a BMD decomposition including the basic elements of the mixture are computed in addition to the single elements/materials least-squares evaluation. If the mixture exhibits the lowest residual, in stage (iv) the BMD is performed considering a mixture of 2 (or more) k-edge elements and water.

3. Results and discussion

Figure 4 shows the water (non-contrast), I, Ba, and Gd images obtained with the conventional BMD algorithm for all the considered processing pipelines. When considering the water images, it can be observed that both the single-pass and two-pass denoising approaches show an effective improvement in the visibility of the main features, such as e.g., brain and soft tissues as well as

Optics EXPRESS

the plastic holder. On the other hand, these features are masked by the noise in the non-processed images. Referring to the I, Ba, and Gd images, spurious signals arising from contamination between the reconstruction channels can be observed. This effect is evident for non denoised images where concentrations of Gd are observed in correspondence of the soft tissues and in correspondence of the I and Ba pipettes. A similar issue can be observed for I and Ba images. As for the denoised images, the effect of contamination among the channels is strongly reduced. However, the applied denoising does not remove the contamination between I and Ba images, where a non negligible percentage of Ba is detected in the pipette containing I and vice versa. This effect can be ascribed to the spectral cross-talk between the two channels due to the limited energy resolution (around 4 keV at 33 keV) which hampers a sharp separation between the two k-edges (close in energy) of I and Ba (Algorithm 1).

Algorithm 1. Minimum-residual basis material decomposition (MR-BMD)

procedure MR-BMD($V(\vec{v}, E)$)

  $M_I \leftarrow$ getBasis(E, I) ▷ Get decomposition basis according to spectrum E
  $M_{Ba} \leftarrow$ getBasis(E, Ba)
  $M_{Gd} \leftarrow$ getBasis(E, Gd)
  $M_{bone} \leftarrow$ getBasis$(E, bone)$
  $M_{H_2O} \leftarrow$ getBasis(E, H_2O)

  for all $\vec{v} \in V(\vec{v}, E)$ **do** ▷ For each voxel in the volume

    $S_I(\vec{v}), r_I(\vec{v}) \leftarrow$ decompose$(V(\vec{v}, E), M_I)$ ▷ Get also the norm residual r
    $S_{Ba}(\vec{v}), r_{Ba}(\vec{v}) \leftarrow$ decompose$(V(\vec{v}, E), M_{Ba})$
    $S_{Gd}(\vec{v}), r_{Gd}(\vec{v}) \leftarrow$ decompose$(V(\vec{v}, E), M_{Gd})$
    $S_{bone}(\vec{v}), r_{bone}(\vec{v}) \leftarrow$ decompose$(V(\vec{v}, E), M_{bone})$
    $S_{H_2O}(\vec{v}), r_{H_2O}(\vec{v}) \leftarrow$ decompose$(V(\vec{v}, E), M_{H_2O})$

    $m(\vec{v}) \leftarrow min\{r_I(\vec{v}), r_{Ba}(\vec{v}), r_{Gd}(\vec{v}), r_{bone}(\vec{v}), r_{H_2O}(\vec{v})\}$ ▷ Find minimum r

    if $m(\vec{v}) == r_I(\vec{v})$ **then** ▷ If minimum residual is for I
      $S_I(\vec{v}), S_{H_2O}(\vec{v}) \leftarrow$ decompose$(V(\vec{v}, E), M_I, M_{H_2O})$ ▷ Decompose I and H_2O
    else if $m(\vec{v}) == r_{Ba}(\vec{v})$ **then**
      $S_{Ba}(\vec{v}), S_{H_2O}(\vec{v}) \leftarrow$ decompose$(V(\vec{v}, E), M_{Ba}, M_{H_2O})$
    else if $m(\vec{v}) == r_{Gd}(\vec{v})$ **then**
      $S_{Gd}(\vec{v}), S_{H_2O}(\vec{v}) \leftarrow$ decompose$(V(\vec{v}, E), M_{Gd}, M_{H_2O})$
    else if $m(\vec{v}) == r_{bone}(\vec{v})$ **then**
      $S_{bone}(\vec{v}) \leftarrow$ decompose$(V(\vec{v}, E), M_{bone})$
    else if $m(\vec{v}) == r_{H_2O}(\vec{v})$ **then**
      $S_{H_2O}(\vec{v}) \leftarrow$ decompose$(V(\vec{v}, E), M_{H_2O})$ ▷ Decompose only H_2O

Figure 5 shows the water, bone, I, Ba, and Gd images obtained with the proposed MR-BMD algorithm for all the considered processing pipelines. If compared to the images reconstructed with conventional BMD, the images reconstructed with MR-BMD (see Fig. 5) show a clear improvement of their global quality even for the case without any additional denoising processing. In particular, contamination among the channels results strongly reduced in I, Ba, and Gd MR-BMD images. Single-pass and two-pass denoising further improve the image quality by reducing the noise.

Optics EXPRESS

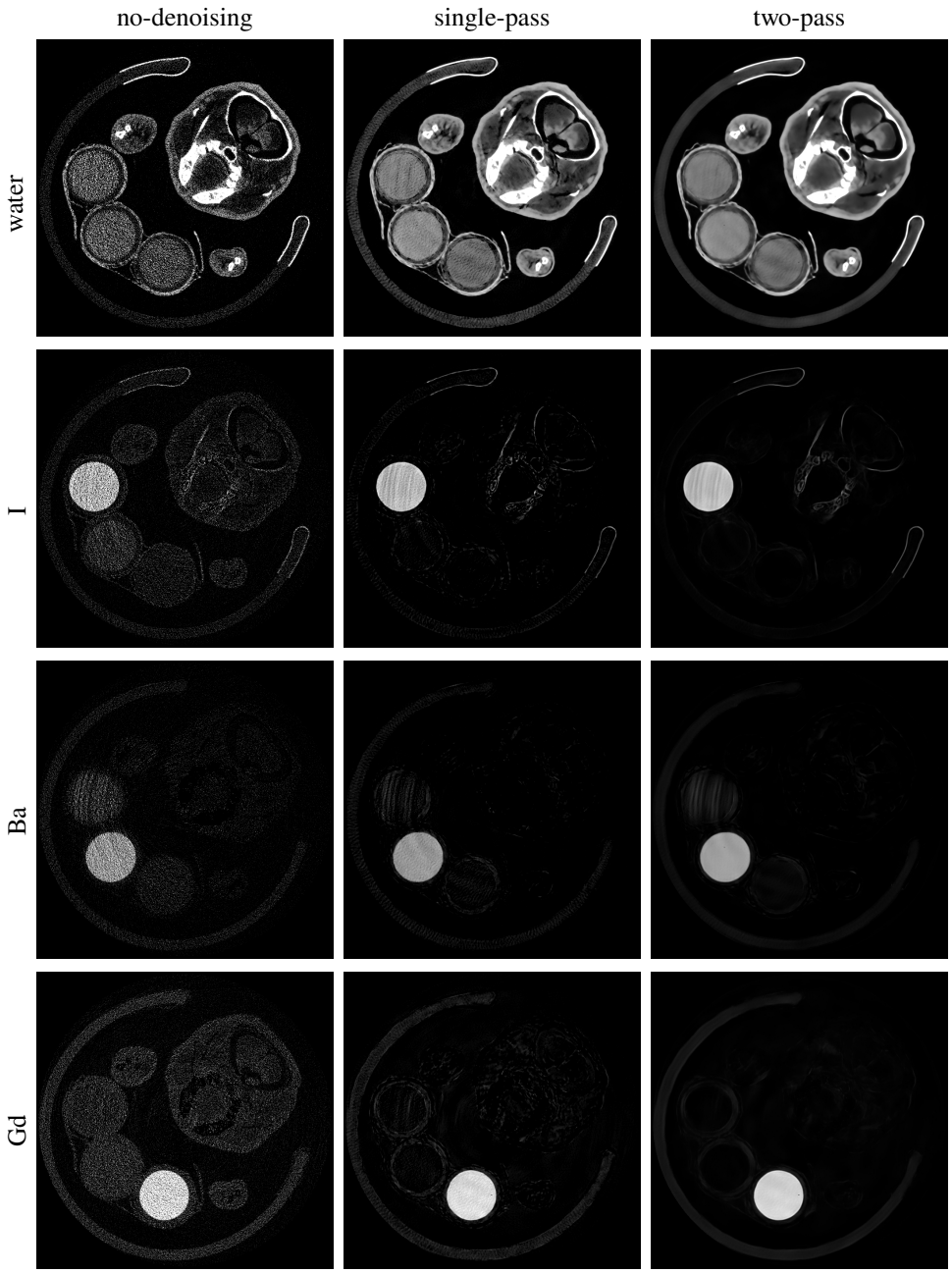

Fig. 4. Results of the conventional multi-material basis decomposition on a representative axial slice obtained according to the three considered approaches: without any denoising step (left column); with a single-pass denoising (center); and with the proposed two-pass denoising (right column).

Optics EXPRESS

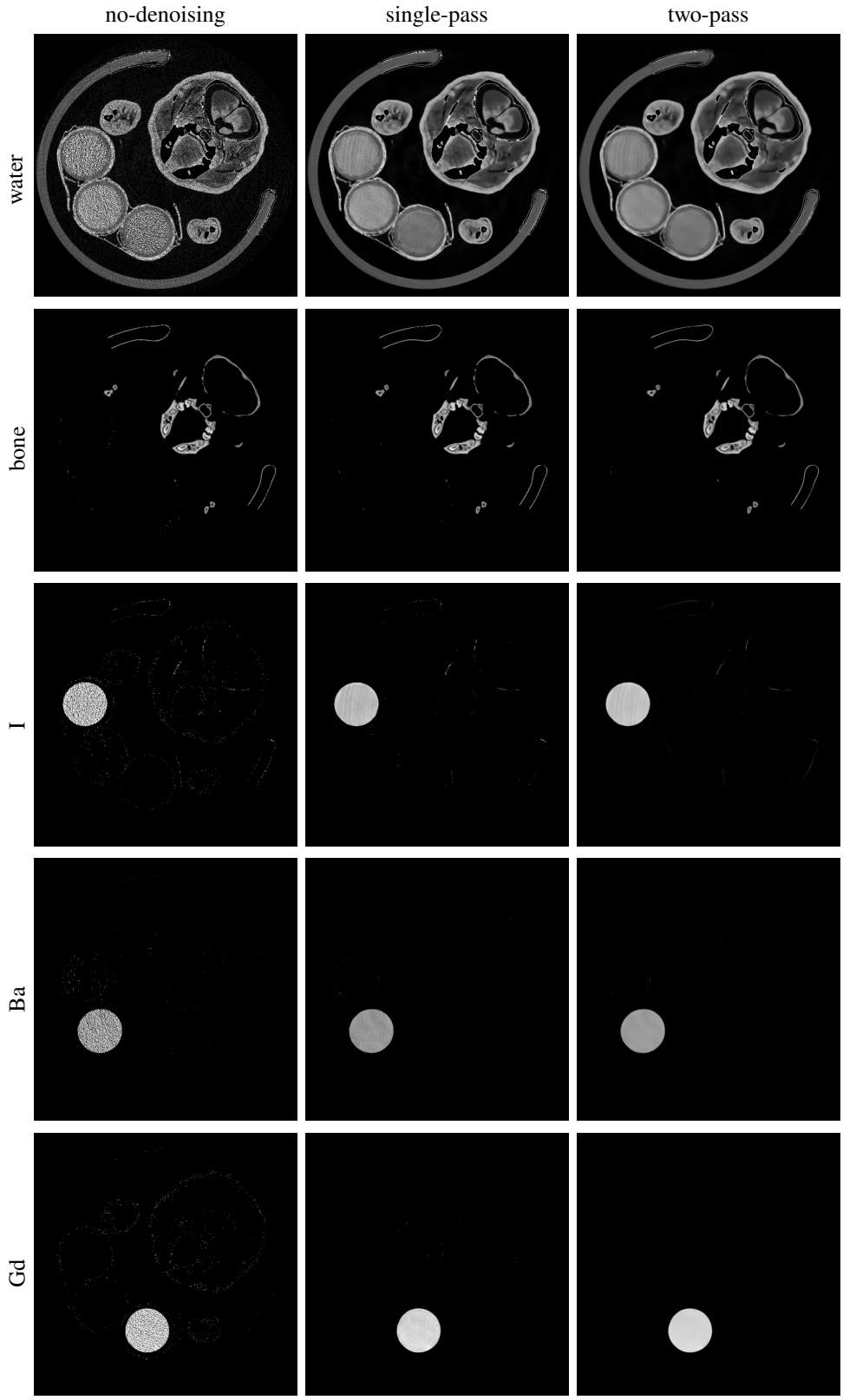

Fig. 5. Results of the proposed minimum-residual multi-material basis decomposition (MR-BMD) on a representative axial slice obtained according to the three considered approaches: without any denoising step (left column); with a single-pass denoising (center); and with the proposed two-pass denoising (right column).

Optics EXPRESS

To better assess the effectiveness of both the denoising approaches and the proposed MR-BMD algorithm, for the 3 pipettes filled with I, Ba, and Gd, the signal and noise have been quantified as the mean and the standard deviations measured over a circular region of interest (ROI) having a diameter of 86 pixels. The results are reported in Table 1, and they are averaged over a few consecutive axial slices. Table 1 reports also for each contrast agent the maximum value between the other two ROIs mean value as an estimate of the contamination among the reconstruction channels. This contamination, intended as spurious signals arising from cross-talk between the decomposed images, is systematic. In particular, for Gd images the contamination equally comes from the other two contrast agents, I and Ba. Conversely, the maximum contamination for I images comes from Ba and vice versa. This latter effect is more evident and is mainly due to the fact that I and Ba k-edges are not sharply separated by the PCD with an energy resolution comparable to the energy gap between their k-edges.

Table 1. Quantitative spectral results for the three k-edge elements (I, Ba, Gd): *S* is the signal measured as the average value of a ROI, *N* is the noise measured as standard deviation in a ROI, *SNR* = *S*/*N*, *R* is the contamination measured as described in the text, Δ is the variation from the nominal values (I=40 mg/ml , Ba=35 mg/ml, Gd=39 mg/ml). Errors come from the consideration of multiple axial slices.

I		S [mg/ml]	N [mg/ml]	SNR	R [mg/ml]	Δ [%]
no-denoising	standard	34.4 ± 0.2	15.0 ± 0.1	2.3	7.1 ± 0.1	−14%
	MR-BMD	36.4 ± 0.1	15.0 ± 0.1	2.4	0.2 ± 0.1	−9%
single-pass	standard	35.6 ± 0.3	3.5 ± 0.1	10	0.5 ± 0.1	−11%
	MR-BMD	36.4 ± 0.2	1.9 ± 0.1	19	0.0 ± 0.0	−9%
two-pass	standard	36.3 ± 0.4	1.7 ± 0.2	21	0.4 ± 0.0	−9%
	MR-BMD	37.8 ± 0.2	0.9 ± 0.1	42	0.0 ± 0.0	−5%
Ba						
no-denoising	standard	28.5 ± 0.1	12.0 ± 0.4	2.4	7.8 ± 0.2	−19%
	MR-BMD	30.1 ± 0.2	12.7 ± 0.4	2.4	0.2 ± 0.1	−14%
single-pass	standard	29.5 ± 0.2	2.1 ± 0.1	14	2.7 ± 0.3	−16%
	MR-BMD	29.4 ± 0.1	1.6 ± 0.1	19	0.0 ± 0.0	−16%
two-pass	standard	31.4 ± 0.2	1.0 ± 0.1	30	4.2 ± 0.4	−10%
	MR-BMD	30.6 ± 0.1	0.7 ± 0.1	47	0.0 ± 0.0	−13%
Gd						
no-denoising	standard	43.8 ± 0.3	15.2 ± 0.2	2.9	7.6 ± 0.2	12%
	MR-BMD	40.4 ± 0.2	16.7 ± 0.1	2.4	0.0 ± 0.0	4%
single-pass	standard	42.7 ± 0.4	1.8 ± 0.2	24	0.9 ± 0.2	9%
	MR-BMD	42.1 ± 0.3	1.5 ± 0.1	28	0.0 ± 0.0	8%
two-pass	standard	40.8 ± 0.4	0.8 ± 0.2	49	0.3 ± 0.1	5%
	MR-BMD	41.7 ± 0.2	0.6 ± 0.1	70	0.0 ± 0.0	7%

Results reported in Table 1 show that independently from the specific decomposition algorithm, the single-pass denoising considerably increases the signal-to-noise ratio (SNR). Moreover, if compared to the single-pass approach, the two-pass denoising leads to another considerable increase in SNR. Comparing the two decomposition algorithms, the MR-BMD outperforms the standard BMD by generally allowing for an improved SNR, a reduced (practically negligible) contamination among the I, Ba, and Gd channels, and providing a quantitative estimation of the concentration of the k-edge elements which is closer to the nominal values. Additionally, the gain in SNR due to the single-pass/two-pass denoising is more evident in the images reconstructed

Optics EXPRESS

with the MR-BMD algorithm. This means that the MR-BMD algorithm performs better when considering as input denoised images. The more accurate material separation allows also for an easy (without additional image processing) volume rendering of all the superimposed images as shown in Fig. 6.

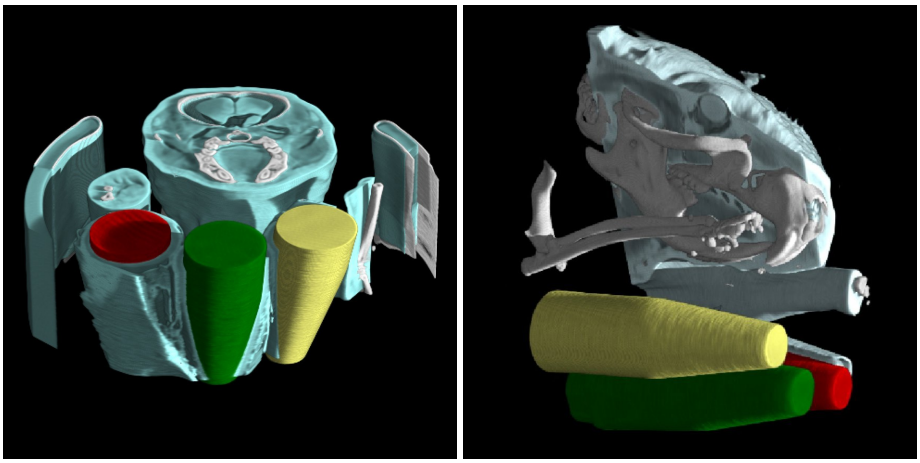

(a) (b)

Fig. 6. Two different views of a volume rendering of the considered sample after two-pass denoising and MR-BMD. Each decomposed material is represented with a different pseudo-color: bone (white), water (cyan), I (red), Ba (green), Gd (yellow). Water (non-contrast) image is partially cut and in b) the sample holder has been virtually removed.

It is important to notice that while for the MR-BMD (Fig. 4) five materials were decomposed (i.e., water, bone, I, Ba, and Gd), only four materials were decomposed via standard BMD (Fig. 5). The bone image was not derived in this case since a straightforward application of the BMD algorithm without any constraint leads to unsuitable noisy images. The different number of decomposed materials does not affect the comparison between the two algorithms. In fact, as described in sect 2.3, the MR-BMD algorithm is designed to use a variable number of bases for each input voxel.

To better explain the advantages of the proposed MR-BMD over the standard BMD approach it is worth focusing on the noise-transfer behaviour of the least-squares solution behind the BMD approach. Generally, the BMD algorithm has to face two main noise challenges. First, considering a fixed X-rays fluence, the SNR of input images decreases with the number n of the selected energy bins, since each energy bin will collect a reduced number of photons. Secondly, the least-squares solution of Eq. (3) is an ill-conditioned problem, meaning that small changes in the matrix to be inverted or in the input data induce large errors in the resulting densities, i.e. an increased noise in the decomposed images. A measure of the degree of ill-conditioning of a matrix is provided by the condition number k which for a given matrix $\mathbf{M}$ having m rows and n columns is defined as the product of the infinity norms of the matrix $\mathbf{M}$ and its inverse $\mathbf{M^{-1}}$:

$$k(M) = \|M\|_\infty \cdot \|M^{-1}\|_\infty \tag{4}$$

being the infinity norm the maximum value of the summed rows of the $\mathbf{M}$ matrix: $\|M\|_\infty = max_i \{\sum_{j=1}^{m} M_{ij}\}$. Values of k close to 1 represent a well-posed problem, while values $k>>1$ measure ill-conditioned matrices. From the formulation of the condition number it is easy to understand how the solution of Eq. (3) moves away from a well-posed problem as the number of selected bases increases. Another source of ill-conditioning for the BMD algorithm arises

Optics EXPRESS

when the selected bases (elements or materials) feature similar weighted attenuation coefficients in most of the selected energy bins. This is the case of small k-edge element concentrations in water featuring k-edge jumps close in energy (e.g. I and Ba) or tissues with similar chemical composition detected by PCDs with a finite energy resolution. In such cases, numerical overlaps between the columns of matrix **M** can occur, thus impairing the linear independence of the elements by inducing a near-singular-matrix behavior. In terms of material decomposition, the ill-conditioning of the BMD problem can be therefore observed as an increased noise in the decomposed images, but also in increased contamination between the channels due to similar attenuation behavior in the employed energy range. To be more specific, referring to the experimental case here presented, the condition number of the matrix employed for the standard BMD is $k(M_{\{H_2O,I,Ba,Gd\}}) \approx 852$. In this case, the high value of the condition number ($\gg 1$) is mainly due to the coexistence of I and Ba, whose k-edges are not sharply separated by the employed PCD. The removal of I from the BMD matrix would, in fact, allow for a reduction of the condition number to $k(M_{\{H_2O,Ba,Gd\}}) \approx 452$ at the cost of a loss of information, since I concentrations would be misinterpreted as Ba signals. The introduction of the bone basis is, instead, responsible for a further increase of the condition number $k(M_{\{H_2O,I,Ba,Gd,bone\}}) \approx 1600$, which leads to noisy images, also affected by signals contamination between the reconstructed channels.

In contrast with the standard BMD algorithm where the decomposition matrix **M** is fixed for the whole reconstruction volume, the MR-BMD algorithm proposes an adaptive decomposition matrix which exploits the information provided by the multiple energy bins. In particular, by setting the energy thresholds of the PCD at the k-edges of the employed contrast agents, the algorithm is sensitive to the k-edge jump (see step ii sect. 2.3), thus allowing to detect the proper k-edge element prior the material decomposition (step iv sect. 2.3). Therefore, if compared to the basic BMD, the MR-BMD totally removes possible contamination between the bases images due to the similar weighted attenuation coefficients. Furthermore, all the collected energy bins can be exploited to discriminate between materials featuring a similar energy-dependent behavior for the weighted mass-absorption coefficients, such as in the case of bone and water bases in our experimental data set. The MR-BMD uses a reduced set of bases accordingly to the identified material in each voxel. In particular, the material decomposition is performed with 2 bases in presence of k-edge elements (water, k-edge element) and with a single element/material for all the other cases (e.g. only bone or water). The main advantage of this approach is that of reducing the number of bases, thus bringing the solution of Eq. (3) closer to a well-posed problem by locally reducing the condition number for **M**. Referring to the experimental case here presented, in the MR-BMD decomposition the condition number of a single material is trivially $k = 1$, since the decomposition matrix reduces to a 1D vector which size equals the number of energy bins. For the I, Ba, and Gd elements, the condition numbers are respectively $K(M_{H_2O,I}) \approx 230$, $K(M_{H_2O,Ba}) \approx 190$, and $K(M_{H_2O,Gd}) \approx 150$, smaller than the condition number of decomposition matrices of the standard BMD.

The experimental results reported here demonstrate that the combination of convolutional neural network denoising approaches with the MR-BMD algorithm allow for a sharp separation of elements with k-edges close in energy with improved SNR performance if compared to the basic non-denoised approach with the standard BMD approach. It is worth mentioning that the vast majority of published literature in the field of quantitative spectral photon counting CT with two (or more) contrast agents, typically focuses onto I and Gd only [7,22,53] and in most cases detectors with large pixel size ($> 100\times100$ μm^2) are employed. A key point of our proposed hardware and software solution is the capability to offer high spatial resolution images (even below the considered 45×45 μm^2) by increasing the cone beam magnification. This allow for *ex vivo* high-resolution studies, in principle limited only by the X-ray source size. At the same time, the high spatial resolution can benefit of a high energy resolution, which combined with

Optics EXPRESS

the proposed MR-BMD algorithm allow for a sharp isolation of Ba and I with k-edges close in energy. This conclusion holds for two generic elements having their K-Edge separated by $\gtrapprox 4$ keV (within the energy range of the incident spectrum).

This work was designed for *ex vivo* studies, therefore a discussion about radiation dose and scanning time is not included. However, while the consideration of *Noise2Noise* requires projection repetition, it is worth noting that the proposed single-pass denoising is compatible with continuous acquisition schemes and therefore its potential use for *in vivo* studies is envisaged.

As pointed out in the original work [35], other convolutional neural networks can be used for *Noise2Inverse* and *Noise2Noise*, such as e.g. MSD, u-net and DnCNN and this might slightly affect the results in terms of denoising. Most significantly, the choice of the network affects computational time and MSD is in most cases the slowest solution. However, as stated in [35], MSD is the most stable approach and therefore the tuning of hyperparameters (mainly the number of epochs used during the training) is usually easier. It is also the approach requiring less memory, so MSD-based denoising can be executed with GPUs having a limited amount of on-board memory.

4. Conclusions

This work presents an optimized workflow for high-resolution multi-material spectral CT using eight energy bins acquired with an X-ray setup implementing the CdTe Pixirad/Pixie-III PCD. The proposed workflow includes: (i) an accurate modeling of the spectral response; (ii) an improved algorithm for material decomposition (MR-BMD); (iii) and two denoising approaches to improve the quality of decomposed images.

In this work, the limiting factors of spectral decomposition, namely noise amplification and cross-talk between decomposed images, have been tackled with two synergistic approaches. First, the modified version of the BMD algorithm, which exploits all the available energy bins to minimize the number of bases used for material decomposition on a single voxel basis, has been designed. Secondly, two advanced denoising approaches have been adopted: a single-pass approach applies Noise2Inverse algorithm to reduce the noise in input to the considered BMD algorithms; the two-pass denoising further reduces the noise in output to improve the SNR in decomposed images by applying Noise2Noise approach in decomposed images.

The effectiveness of denoising strategies and the proposed MR-BMD have been demonstrated through experimental acquisitions of a mouse specimen together with three cuvettes separately filled with different contrast agents (I, Ba, and Gd) commonly employed for medical applications.

Results show that, for the same denoising approach, the MR-BMD algorithm outperforms the conventional BMD. In particular, MR-BMD allows removing signal cross-talks between I, Ba, and Gd decomposed images, affecting the conventional BMD algorithm. This effect is particularly evident between I and Ba elements, whose k-edges close in energy are not sharply separated by the PCD. An additional advantage of MR-BMD also arises from the possibility of decomposing an indefinite number of bases without loss in noise response, thanks to its adaptive approach based on a material recognition step prior to the actual decomposition.

Both BMD and MR-BMD take advantage of the adopted denoising approaches. However, the benefits of MR-BMD over the standard BMD are further enhanced when denoising is applied. As an example, for I images, if compared to the non-denoised, the single-pass approach increases the SNR by a factor of 4.4 for the standard BMD and 7.8 for the MR-BMD. This relative gain in SNR, which correspond to an equivalent increased input statistics of about $\times 19$ (for BMD) and $\times 61$ (for MR-BMD), can be employed to either reduce the delivered dose or increase the visibility of small contrast agent concentrations. Furthermore, compared to the single-pass denoising, the double-pass approach further increases the SNR response of an additional factor of 2, corresponding to an additional 4-fold increased statistics over the single-pass step. In this

Optics EXPRESS

context, additional research will be dedicated to assessing the minimum concentration detectable by our approach as well as its sensitivity when mixtures of two or more contrast agents are used.

Funding. Commissione Scientifica Nazionale 5, Instituto Nazionale di Fisica Nucleare (22260/2020).

Acknowledgments. V. Di Trapani would like to acknowledge the S-BaXIT project, funded by the European Research Council (ERC) under the European Union's Horizon 2020 research and innovation program (Grant agreement n. 866026). Authors would like to thank Allard Hendriksen (CWI, Amsterdam) for freely distributing a Python implementation of *Noise2Inverse*.

Disclosures. The authors declare no conflicts of interest.

Data availability. Sample data as well as MATLAB and Python code considered for this work are freely available at [54].

References

1. M. Willemink, M. Persson, A. Pourmorteza, N. Pelc, and D. Fleischmann, "Photon-counting CT: Technical principles and clinical prospects," Radiology **289**(2), 293–312 (2018).
2. S. S. Hsieh, S. Leng, K. Rajendran, S. Tao, and C. H. McCollough, "Photon Counting CT: Clinical Applications and Future Developments," IEEE Trans. Radiat. Plasma Med. Sci. **5**(4), 441–452 (2021).
3. J. R. Ashton, J. L. West, and C. T. Badea, "In vivo small animal micro-CT using nanoparticle contrast agents," Front. Pharmacol. **6**, 256 (2015).
4. B. M. Yeh, P. F. FitzGerald, P. M. Edic, J. W. Lambert, R. E. Colborn, M. E. Marino, P. M. Evans, J. C. Roberts, Z. J. Wang, M. J. Wong, and P. J. Bonitatibus, "Opportunities for new CT contrast agents to maximize the diagnostic potential of emerging spectral CT technologies," Adv. Drug Delivery Rev. **113**, 201–222 (2017).
5. C. Badea, D. Clark, M. Holbrook, M. Srivastava, Y. Mowery, and K. Ghaghada, "Functional imaging of tumor vasculature using iodine and gadolinium-based nanoparticle contrast agents: a comparison of spectral micro-CT using energy integrating and photon counting detectors," Phys. Med. Biol. **64**(6), 065007 (2019).
6. R. Symons, T. Cork, M. Lakshmanan, R. Evers, C. Davies-Venn, K. Rice, M. Thomas, C.-Y. Liu, S. Kappler, S. Ulzheimer, V. Sandfort, D. Bluemke, and A. Pourmorteza, "Dual-contrast agent photon-counting computed tomography of the heart: initial experience," Int. J. Cardiovasc Imaging **33**(8), 1253–1261 (2017).
7. D. Muenzel, D. Bar-Ness, E. Roessl, I. Blevis, M. Bartels, A. Fingerle, S. Ruschke, P. Coulon, H. Daerr, F. Kopp, B. Brendel, A. Thran, M. Rokni, J. Herzen, L. Boussel, F. Pfeiffer, R. Proksa, E. Rummeny, P. Douek, and P. Noël, "Spectral photon-counting ct: Initial experience with dual-contrast agent k-edge colonography," Radiology **283**(3), 723–728 (2017).
8. R. Symons, B. Krauss, P. Sahbaee, T. E. Cork, M. N. Lakshmanan, D. A. Bluemke, and A. Pourmorteza, "Photon-counting CT for simultaneous imaging of multiple contrast agents in the abdomen: an in vivo study," Med. Phys. **44**(10), 5120–5127 (2017).
9. D. Muenzel, H. Daerr, R. Proksa, A. Fingerle, F. Kopp, P. Douek, J. Herzen, F. Pfeiffer, E. Rummeny, and P. Noël, "Simultaneous dual-contrast multi-phase liver imaging using spectral photon-counting computed tomography: a proof-of-concept study," Eur. Radiol. Exp. **1**(1), 25 (2017).
10. S. Si-Mohamed, A. Thivolet, P.-E. Bonnot, D. Bar-Ness, V. Kepenekian, D. Cormode, P. Douek, and P. Rousset, "Improved Peritoneal Cavity and Abdominal Organ Imaging Using a Biphasic Contrast Agent Protocol and Spectral Photon Counting Computed Tomography K-Edge Imaging," Invest. Radiol. **53**(10), 629–639 (2018).
11. L. Ren, N. Huber, K. Rajendran, J. Fletcher, C. McCollough, and L. Yu, "Dual-Contrast Biphasic Liver Imaging With Iodine and Gadolinium Using Photon-Counting Detector Computed Tomography: An Exploratory Animal Study," Invest. Radiol. **57**(2), 122–129 (2022).
12. N. Anderson, A. Butler, N. Scott, N. Cook, J. Butzer, N. Schleich, M. Firsching, R. Grasset, N. Ruiter, M. Campbell, and P. Butler, "Spectroscopic (multi-energy) CT distinguishes iodine and barium contrast material in MICE," Eur. Radiol. **20**(9), 2126–2134 (2010).
13. M. Ruat and C. Ponchut, "Defect signature, instabilities and polarization in cdte x-ray sensors with quasi-ohmic contacts," J. Instrum. **9**(04), C04030 (2014).
14. T. Billoud, C. Leroy, C. Papadatos, M. Pichotka, S. Pospisil, and J. Roux, "Homogeneity study of a GaAs:cr pixelated sensor by means of x-rays," J. Instrum. **13**(04), P04002 (2018).
15. P. Delogu, L. Brombal, V. Trapani, S. Donato, U. Bottigli, D. Dreossi, B. Golosio, P. Oliva, L. Rigon, and R. Longo, "Optimization of the equalization procedure for a single-photon counting cdte detector used for ct," J. Instrum. **12**(11), C11014 (2017).
16. V. Di Trapani and F. Brun, "Pre-and post-reconstruction digital image processing solutions for computed tomography with spectral photon counting detectors," Nucl. Instrum. Methods Phys. Res., Sect. A **1010**, 165510 (2021).
17. L. Brombal, S. Donato, F. Brun, P. Delogu, V. Fanti, P. Oliva, L. Rigon, V. Di Trapani, R. Longo, and B. Golosio, "Large-area single-photon-counting CdTe detector for synchrotron radiation computed tomography: a dedicated pre-processing procedure," J. Synchrotron Radiat. **25**(4), 1068–1077 (2018).
18. R. Ballabriga, J. Alozy, G. Blaj, M. Campbell, M. Fiederle, E. Fröjdh, E. Heijne, X. Llopart, M. Pichotka, S. Procz, L. Tlustos, and W. Wong, "The Medipix3RX: a high resolution, zero dead-time pixel detector readout chip allowing spectroscopic imaging," J. Instrum. **8**(02), C02016 (2013).

Optics EXPRESS

19. R. Bellazzini, A. Brez, G. Spandre, M. Minuti, M. Pinchera, P. Delogu, P. De Ruvo, and A. Vincenzi, "PIXIE III: a very large area photon-counting CMOS pixel ASIC for sharp X-ray spectral imaging," J. Instrum. **10**(01), C01032 (2015).
20. R. E. Alvarez and A. Macovski, "Energy-selective reconstructions in x-ray computerised tomography," Phys. Med. Biol. **21**(5), 733–744 (1976).
21. B. Heismann, B. Schmidt, and T. Flohr, *Spectral computed tomography* (2012).
22. B. Xie, T. Su, V. Kaftandjian, P. Niu, F. Yang, M. Robini, Y. Zhu, and P. Duvauchelle, "Material decomposition in x-ray spectral ct using multiple constraints in image domain," J. Nondestruct. Eval. **38**(1), 16 (2019).
23. Z. Li, S. Leng, L. Yu, A. Manduca, and C. H. McCollough, "An effective noise reduction method for multi-energy CT images that exploit spatio-spectral features," Med. Phys. **44**(5), 1610–1623 (2017).
24. J. Butzer, A. Butler, P. Butler, P. Bones, N. Cook, and L. Tlustos, "Medipix imaging-evaluation of datasets with PCA," in *2008 23rd International Conference Image and Vision Computing New Zealand*, (IEEE, 2008), pp. 1–6.
25. C. Mory, B. Sixou, S. Si-Mohamed, L. Boussel, and S. Rit, "Comparison of five one-step reconstruction algorithms for spectral CT," Phys. Med. Biol. **63**(23), 235001 (2018).
26. N. R. Fredette, A. Kavuri, and M. Das, "Multi-step material decomposition for spectral computed tomography," Phys. Med. Biol. **64**(14), 145001 (2019).
27. D. P. Clark and C. T. Badea, "Hybrid spectral CT reconstruction," PLoS One **12**(7), e0180324 (2017).
28. W. Wu, D. Hu, C. Niu, L. V. Broeke, A. P. Butler, P. Cao, J. Atlas, A. Chernoglazov, V. Vardhanabhuti, and G. Wang, "Deep learning based spectral CT imaging," Neural Networks **144**, 342–358 (2021).
29. B. Zhao, H. Ding, Y. Lu, G. Wang, J. Zhao, and S. Molloi, "Dual-dictionary learning-based iterative image reconstruction for spectral computed tomography application," Phys. Med. Biol. **57**(24), 8217–8229 (2012).
30. W. Fang, D. Wu, K. Kim, M. Kalra, R. Singh, L. Li, and Q. Li, "Iterative material decomposition for spectral CT using self-supervised Noise2Noise prior," Phys. Med. Biol. **66**(15), 155013 (2021). Cited By 0.
31. K. Zhang, W. Zuo, Y. Chen, D. Meng, and L. Zhang, "Beyond a Gaussian denoiser: Residual learning of deep CNN for image denoising," IEEE Trans. on Image Process. **26**(7), 3142–3155 (2017).
32. J. Lehtinen, J. Munkberg, J. Hasselgren, S. Laine, T. Karras, M. Aittala, and T. Aila, "Noise2Noise: Learning image restoration without clean data," (2018), pp. 4620–4631.
33. J. Batson and L. Royer, "Noise2Seif: Blind denoising by self-supervision," (2019), pp. 826–835.
34. A. Krull, T.-O. Buchholz, and F. Jug, "Noise2void-Learning denoising from single noisy images," (2019), pp. 2124–2132.
35. A. Hendriksen, D. Pelt, and K. Batenburg, "Noise2Inverse: Self-Supervised Deep Convolutional Denoising for Tomography," IEEE Trans. Comput. Imaging **6**, 1320–1335 (2020).
36. A. Hendriksen, M. Bührer, L. Leone, M. Merlini, N. Vigano, D. Pelt, F. Marone, M. di Michiel, and K. Batenburg, "Deep denoising for multi-dimensional synchrotron X-ray tomography without high-quality reference data," Sci. Rep. **11**(1), 11895 (2021).
37. N. Yuan, J. Zhou, and J. Qi, "Half2Half: deep neural network based CT image denoising without independent reference data," Phys. Med. Biol. **65**(21), 215020 (2020).
38. F. Brun, V. Trapani, D. Dreossi, R. Longo, P. Delogu, and L. Rigon, "K-edge spectral computed tomography with a photon counting detector and discrete reconstruction," *Conference Proceeding* (2018), 5245–5248.
39. F. Brun, V. Di Trapani, D. Dreossi, L. Rigon, R. Longo, and P. Delogu, "Towards in vivo K-edge X-ray micro-CT with the Pixirad-I/Pixie-III detector," *Conference Proceeding* (2019), 123–126.
40. F. Brun, V. Di Trapani, J. Albers, P. Sacco, D. Dreossi, L. Brombal, L. Rigon, R. Longo, A. Mittone, C. Dullin, A. Bravin, and P. Delogu, "Single-shot K-edge subtraction x-ray discrete computed tomography with a polychromatic source and the Pixie-III detector," Phys. Med. Biol. **65**(5), 055016 (2020).
41. S. Cipiccia, F. Brun, V. Di Trapani, C. Rau, and D. Batey, "Dual energy X-ray beam ptycho-fluorescence imaging," J. Synchrotron Radiat. **28**(6), 1916–1920 (2021).
42. F. Brun, V. Di Trapani, D. Batey, S. Cipiccia, and C. Rau, "Edge-subtraction X-ray ptychographic imaging with pink beam synchrotron radiation and a single photon-counting detector," Sci. Rep. **10**(1), 6526 (2020).
43. V. Sriskaran, J. Alozy, R. Ballabriga, M. Campbell, N. Egidos, J. Fernandez-Tenllado, E. Heijne, I. Kremastiotis, A. Koukab, X. Llopart, J. Sallese, and L. Tlustos, "New architecture for the analog front-end of Medipix4," Nucl. Instrum. Methods Phys. Res., Sect. A **978**, 164412 (2020).
44. V. Di Trapani, A. Bravin, F. Brun, D. Dreossi, R. Longo, A. Mittone, L. Rigon, and P. Delogu, "Characterization of the acquisition modes implemented in Pixirad-1/Pixie-III X-ray Detector: Effects of charge sharing correction on spectral resolution and image quality," Nucl. Instrum. Methods Phys. Res., Sect. A **955**, 163220 (2020).
45. L. Feldkamp, L. Davis, and J. Kress, "Practical cone-beam algorithm," J. Opt. Soc. Am. A **1**(6), 612–619 (1984).
46. G. Wang, "X-ray micro-CT with a displaced detector array," Med. Phys. **29**(7), 1634–1636 (2002).
47. A. Biguri, M. Dosanjh, S. Hancock, and M. Soleimani, "TIGRE: A MATLAB-GPU toolbox for CBCT image reconstruction," Biomed. Phys. Eng. Express **2**(5), 055010 (2016).
48. N. Vo, R. Atwood, and M. Drakopoulos, "Superior techniques for eliminating ring artifacts in X-ray micro-tomography," Opt. Express **26**(22), 28396–28412 (2018).
49. V. Di Trapani, A. Bravin, F. Brun, D. Dreossi, R. Longo, A. Mittone, L. Rigon, and P. Delogu, "Characterization of noise and efficiency of the Pixirad-1/Pixie-III CdTe X-ray imaging detector," J. Instrum. **13**(12), C12008 (2018).

Optics EXPRESS

50. L. Brombal, L. Rigon, F. Arfelli, R. Menk, and F. Brun, "A Geant4 tool for edge-illumination X-ray phase-contrast imaging," J. Instrum. **17**(01), C01043 (2022).
51. L. Brombal, F. Arfelli, F. Brun, F. Longo, N. Poles, and L. Rigon, "X-ray differential phase-contrast imaging simulations with Geant4," J. Phys. D: Appl. Phys. **55**, 045102 (2021).
52. G. Poludniowski, G. Landry, F. Deblois, P. Evans, and F. Verhaegen, "SpekCalc: a program to calculate photon spectra from tungsten anode x-ray tubes," Phys. Med. Biol. **54**(19), N433–N438 (2009).
53. S. Si-Mohamed, D. Bar-Ness, M. Sigovan, V. Tatard-Leitman, D. Cormode, P. Naha, P. Coulon, L. Rascle, E. Roessl, M. Rokni, A. Altman, Y. Yagil, L. Boussel, and P. Douek, "Multicolour imaging with spectral photon-counting ct: a phantom study," Eur. Radiol. Exp. **2**(1), 34 (2018).
54. F. Brun, "Multi-material spectral photon-counting micro-ct with minimum residual decomposition and self-supervised deep denoising," github 2022 [retrieved 9 September 2022], https://github.com/francescobrun/mr-bmd.